Science Advances

Log in • My account • Contact Us
Become a member • Renew my subscription • Sign up for newsletters

RESEARCH ARTICLE | PHYSICAL SCIENCES

Ice-like water supports hydration forces and eases sliding friction

Nishad Dhopatkar[*], Adrian P. Defante[*] and Ali Dhinojwala[†]

+ See all authors and affiliations

PRE Peer Reviewed
← see details

| Article | Figures & Data | Info & Metrics | eLetters | PDF |

Abstract

The nature of interfacial water is critical in several natural processes, including the aggregation of lipids into the bilayer, protein folding, lubrication of synovial joints, and underwater gecko adhesion. The nanometer-thin water layer trapped between two surfaces has been identified to have properties that are very different from those of bulk water, but the molecular cause of such discrepancy is often undetermined. Using surface-sensitive sum frequency generation (SFG) spectroscopy, we discover a strongly coordinated water layer confined between two charged surfaces, formed by the adsorption of a cationic surfactant on the hydrophobic surfaces. By varying the adsorbed surfactant coverage and hence the surface charge density, we observe a progressively evolving water structure that minimizes the sliding friction only beyond the surfactant concentration needed for monolayer formation. At complete surfactant coverage, the strongly coordinated confined water results in hydration forces, sustains confinement and sliding pressures, and reduces dynamic friction. Observing SFG signals requires breakdown in centrosymmetry, and the SFG signal from two oppositely oriented surfactant monolayers cancels out due to symmetry. Surprisingly, we observe the SFG signal for the water confined between the two charged surfactant monolayers, suggesting that this interfacial water layer is noncentrosymmetric. The structure of molecules under confinement and its macroscopic manifestation on adhesion and friction have significance in many complicated interfacial processes prevalent in biology, chemistry, and engineering.

Keywords: coordinated water, hydration forces, friction, surfactants, sum frequency generation

INTRODUCTION

Hydrophobic and hydration forces, encountered in a number of interfacial processes, are presumed to be directly related to the structure and orientation of interfacial water ([1–4]). Two nonpolar surfaces underwater experience a strong, long-range, attractive hydrophobic force due to the release of ordered interfacial molecules promoting intimate contact ([1, 2]). In contrast, an electrostatic double-layer force prevents the contact between two charged surfaces; however, at subnanometer distances, they experience an attractive van der Waals force. Together, these are known as DLVO forces ([5]). For highly charged surfaces or in the presence of high salt concentrations, an additional short-range, monotonically repulsive force is observed, which has been called the hydration force. The origin of this entropically driven hydration force is a bound hydration sheath or the layering of water at the charged interface ([6–8]). Hydration forces were first reported between two charged lipid bilayers, and the magnitude and the decay length of these repulsive forces are often related to either the overlapping of hydrated head groups (steric and protrusion forces) or the undulation forces due to thermal fluctuations of the lipid leaflets ([6, 8–11]). It has been observed by surface force apparatus (SFA) measurements and molecular dynamics (MD) simulations that, under confinement, water exhibits physical properties that differ from those of bulk water ([12–15]). However, direct evidence of the structure of this confined interface and particularly the state of the hydrogen bonding network of the confined water are lacking, which is elementary to understanding the hydration forces in aqueous media.

There has been considerable progress in understanding the structure and dynamics of interfacial water next to hydrophobic or charged surfaces using spectroscopy and MD simulations ([15–20]). The interface-selective infrared-visible sum frequency generation (SFG) spectroscopy experiments have revealed a highly coordinated hydrogen bonding structure of water next to charged surfaces ([21–24]).
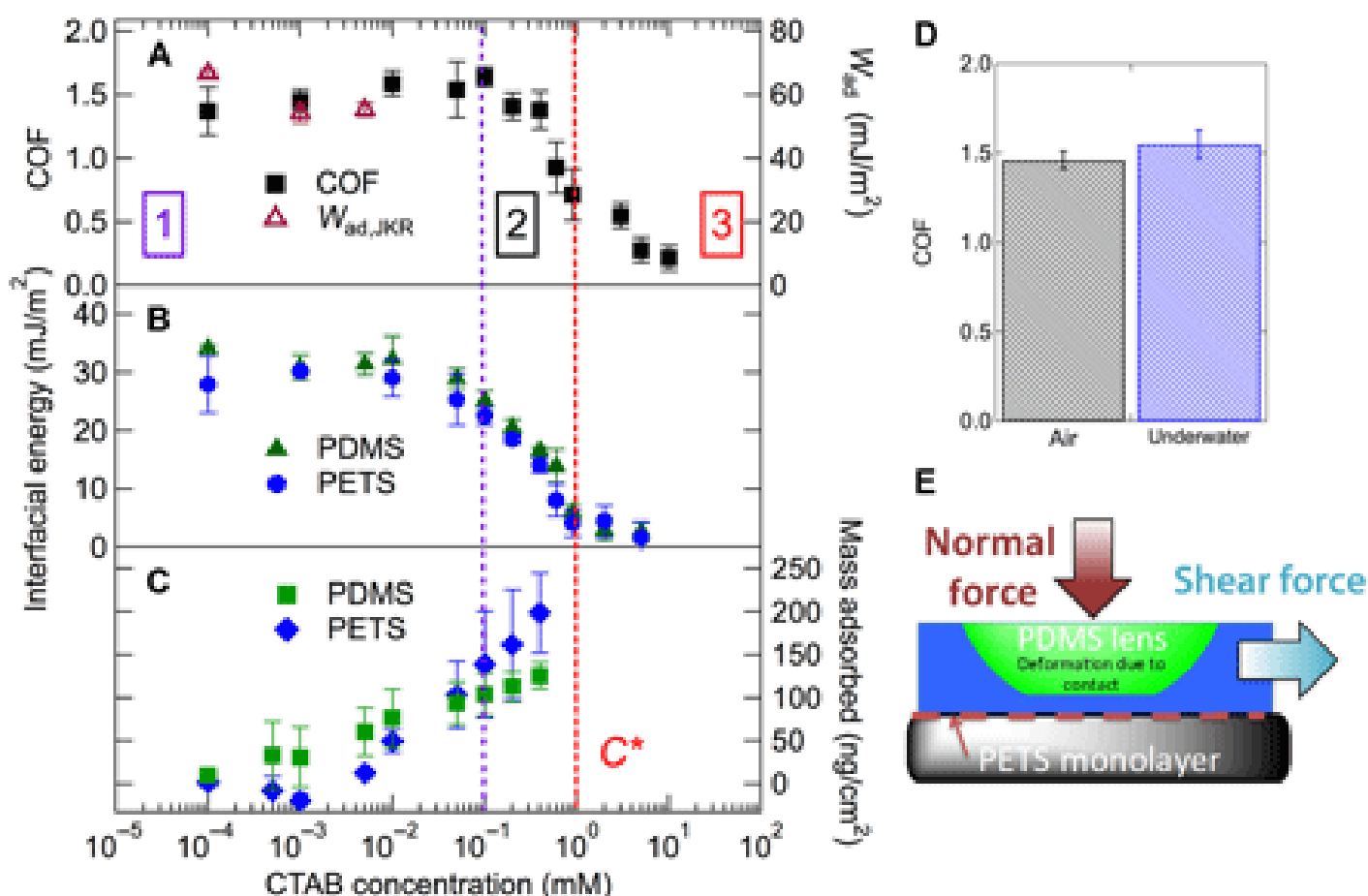
Science Advances

water. Coherent anti-Stokes Raman spectroscopy (CARS) experiments found that the water between the head groups of opposing lipid leaflets of a multilamellar onion-like structure was ordered (27). However, CARS lacks the surface sensitivity to discriminate between bound and unbound water. SFG spectroscopy has been used to interrogate the dry contact interface (28), but no SFG measurement has been reported for the structure of confined water between two charged surfaces.

Here, we used SFG spectroscopy to study the contact interface between two surfactant-covered charged surfaces, elucidating the molecular nature of confined water and its influence on macroscopic underwater friction. By varying the surfactant surface coverage, we could tune the surface charge density and study its effect on the structure of confined water. At low surfactant concentration, we observe a dry contact between two hydrophobic surfaces underwater, which results in a high coefficient of friction (COF). At high surfactant concentrations, we observe a nanometer-thin layer of water maintained by hydration forces between these two surfactant monolayers, which leads to the lowering of COF. The presence of water alone is not sufficient to reduce friction, indicating that a threshold coverage of surfactant adsorption is needed to hold the interstitial water under pressure to promote sliding. The SFG spectroscopy unexpectedly reveals a strongly coordinated structure of confined water, typically seen for ice, between two surfactant monolayer-coated surfaces and that is maintained during the sliding friction. To our knowledge, this is the first direct measurement of the structure of a confined aqueous interface that connects the interfacial molecular structure to surface forces by combining vibrational spectroscopy and contact mechanics.

RESULTS AND DISCUSSION

Figure 1A shows the COF between a polydimethylsiloxane (PDMS) lens and a (phenylethyl)trichlorosilne (PETS) monolayer, sliding underwater at different cetyltrimethyl-ammonium bromide (CTAB) concentrations. For all concentrations studied here, the sliding force is linearly proportional to the normal force (text S1). The magnitude of the changes in the COF is qualitatively similar to that reported by Richards and Roberts (29), who studied friction between two rubber surfaces in the presence of anionic surfactant. We categorize this behavior into three different regions. In region 1, the COF is high (1.55 ± 0.08) and insensitive to the CTAB concentration. In region 2, the COF decreases rapidly with increasing CTAB concentration. In region 3, the COF continues to decrease until 5 mM, before reaching a second plateau (μ = 0.25 ± 0.05). We define this concentration as C^*_{COF}. We define the onset of region 3 as the critical micelle concentration (cmc) of CTAB, the concentration needed for forming a monolayer at the air-water interface. Note that $C^*_{COF} > cmc$. To understand the friction results, it is first necessary to understand the structure of interfacial water and how surfactants adsorb onto hydrophobic surfaces.

Fig. 1 Contact mechanics measurements.

(**A**) Comparison of the underwater COF on the left axis and the work of adhesion (W_{ad}) obtained using zero-load JKR (33) on the right axis. With zero-load JKR, the values were not measurable after 0.005 mM CTAB. The lens did not make adhesive contact past 0.005 mM. (**B** and **C**) The amount of adsorbed CTAB was measured by interfacial energy calculated from contact angle measurements (B) and QCM-D measurements (C), both as a function of surfactant concentration. QCM-D measurements of the mass adsorbed were analyzed using the

ScienceAdvances

root mean square roughness measured by atomic force microscopy is in good agreement the simulation of glass with PETS (on film). The root mean square roughness of glass and a PETS self-assembled monolayer (PETS-SAM) on glass was 2.8 and 3.6 nm, respectively. The dashed lines denote the three regions described in the main text, highlighting the differences between friction and surface coverage. C^* is the concentration at which the monolayer formation is complete, and $C^* \neq C^*_{COF}$. (**D**) The COF in air and underwater without any CTAB serves as control experiments. (**E**) The schematic of a PDMS lens sliding on a PETS substrate is shown to measure the COF (not to scale). The flattened contact under the compressive load is accentuated for clear visualization.

We have determined the adsorption isotherm for CTAB on both PETS and PDMS by calculating the interfacial energy ($\gamma_{s,l}$) on the basis of the contact angle measurements of different CTAB solutions on PETS or PDMS substrates. To calculate the interfacial energy, we independently measured the surface tension ($\gamma_{l,v}$) of the CTAB solutions at the liquid-vapor interface using a Wilhelmy plate balance, and we assumed that the surface energy of the solid ($\gamma_{s,v}$) was constant (text S2) (**30**). **Figure 1B** shows the changes in $\gamma_{s,l}$ with CTAB concentration, which are defined by the three regions described in the friction measurements. In region 1, the values of $\gamma_{s,l}$ for both PETS and PDMS are insensitive to the CTAB concentration, suggesting that, perhaps, CTAB adsorbs minimally in this concentration range. In region 2, $\gamma_{s,l}$ decreases until 0.9 mM CTAB. We identify this point as C^*, the surfactant concentration needed to saturate the surface. C^* is identified to be the same as the cmc, and thus, $C^*_{COF} > C^*$. An observation that $C^*_{PETS} = C^*_{PDMS}$ indicates the similarity in the adsorbed CTAB monolayers on both hydrophobic surfaces. In region 3, the values of $\gamma_{s,l}$ are again independent of surfactant concentration. Using Gibbs surface excess, we estimate the surface coverage (Γ_{CA}) for the surfaces to be $\Gamma_{CA,PDMS} = 116 \pm 18$ ng/cm^2 and $\Gamma_{CA,PETS} = 123 \pm 15$ ng/cm^2 (text S2). These values of surface coverage match the values expected for an adsorbed CTAB monolayer oriented approximately parallel to the surface normal, $\Gamma_\perp = 135$ ng/cm^2 (**31**, **32**). For molecules lying flat or parallel to the surface plane, we expect a coverage of $\Gamma_\parallel = 88$ ng/cm^2 (**31**). These results suggest that a monolayer coverage of surfactant is complete at C^* on both PETS and PDMS substrates with similar surface coverage.

To directly quantify the mass of CTAB adsorbed on PETS and PDMS, we used quartz crystal microbalance with dissipation (QCM-D), as shown in **Fig. 1C**. The data show that in region 1, CTAB adsorbs onto PETS and PDMS, even though the COF is similar to the values observed underwater without any CTAB. Adsorbed mass continues to increase in region 2. The use of the Sauerbrey equation to calculate the adsorbed amount is not valid beyond 0.9 mM CTAB concentration because of the increase in dissipation harmonics (text S3). This concentration, 0.9 mM, coincides with the cmc of purified CTAB and C^*, calculated using the interfacial energy measurements. The increased dissipation suggests that loosely attached micelles are close to the CTAB monolayer in region 3. QCM-D accounts for both adsorbed surfactants and bound water; hence, the surface coverage values measured by QCM-D are higher than those determined from interfacial energy measurements.

To further elucidate the orientation of the adsorbed CTAB monolayer and the structure of interfacial water, we used surface-sensitive infrared-visible SFG spectroscopy in total internal reflection geometry. SFG is a second-order nonlinear optical technique that provides information on chemical composition and orientation of interfacial molecules (**40**). The selection rules of SFG spectroscopy prohibit signals from a centrosymmetric bulk, making it possible to selectively interrogate only the adsorption of CTAB molecules at a PETS interface. In this experiment, a PETS monolayer was deposited on a sapphire prism, and the changes in the SFG spectra are monitored as a function of CTAB concentration underwater. The spectral features in the hydrocarbon region (2750 to 3150 cm^{-1}) with increasing CTAB concentration are shown in **Fig. 2** (A and B). These measurements are done using D$_2$O, instead of H$_2$O, to avoid the overlapping of the narrow features of hydrocarbon signals by the broad spectral signature of H$_2$O. We collected SFG spectra for selected concentrations in region 1 (0.005 mM), region 2 (0.1 and 0.9 mM), and region 3 (5 mM). For PETS-air and PETS-D$_2$O interfaces, the strong peaks observed at 3040 and 3070 cm^{-1} are associated with phenyl ν_{7a} and ν_2 stretching mode vibrations, respectively (**41**). Weaker peaks observed at 2910 and 2970 cm^{-1} are assigned to Si-CH$_2$ and the methylene group connected to the terminal phenyl group, respectively (**42**). The peak assignments are based on infrared and Raman spectroscopy (text S4). The persistence of ordered phenyl groups underwater is consistent with the high interfacial energy measured for the PETS-water interface.

⬇ Download high-res image | ⧉ Open in new tab | ⬇ Download Powerpoint

Fig. 2 SFG spectra for CTAB adsorption on PETS.

(**A** and **B**) SFG spectra collected using SSP (A) and SPS (B) polarization as a function of CTAB concentration, in which we expect hydrocarbon signatures. Measuring both polarizations provides complementary data for the spectral interpretation of CTAB on PETS. (**C**) The presence of D$_2$O was observed by scanning the region where we expected only D$_2$O spectral features. The characteristic regions (1 to 3) are indicated by the vertical bars. The weakly coordinated −OD peak (represented by dashed line with 2) and the strongly coordinated −OD (represented by dashed line with 1) peak evolve with increasing surfactant concentration. (**D**) The spectra were fitted using the Lorentzian function, and the changes in amplitude CH$_{2,asym}$ ($A_{q,2935}$) are shown as a function of surfactant concentration. SPS is more sensitive to the orientational changes of CTAB than SSP. a.u., arbitrary unit. (**E**) Model of the CTAB interface in contact with water. For simplicity, this model assumes 100% dissociation of CTAB head groups, although it has been reported that the dissociation can be as low as 21% (**34**). The surface density of −OH groups on sapphire surface (**35**), molecular dimensions for CTAB (**11**, **36**), water (**37**), and PETS (**38**, **39**) were estimated on the basis of published literature. The orthogonal packing represented is consistent with the area per molecule based on the interfacial energy measurement, 52 Å^2 per molecule, which is similar to the theoretical area calculated for orthogonal packing (text S2).

As we increase the concentration of CTAB, we observe an increase in signal intensity of the 2935-cm^{-1} peak assigned to CH$_{2,asym}$ (**43**, **44**). We also observe this distinct peak in SPS polarization in **Fig. 2B**. In SSP, a weaker signal corresponding to CH$_{3,sym}$ (r$^+$; 2875 cm^{-1}) (**43**–**45**) and a small shoulder for CH$_{2,Fermi}$ (2905 cm^{-1}) (**46**) were also observed in the spectra. Above 0.1 mM CTAB, a peak at 2990 cm^{-1}, opposite in phase with respect to CH$_{2,asym}$, continues to grow stronger and is associated with the symmetric N$^+$-(CH$_3$)$_3$ (**47**) vibrations from the CTAB head group. The increasing amplitude of r$^+$ mode (CH$_{3,sym}$; 2875 cm^{-1}) with CTAB concentration and the absence of d$^+$ (CH$_{2,sym}$; 2850 cm^{-1}) mode suggest the formation of a well-ordered CTAB monolayer on the PETS-coated surface.

is consistent with the results from the interfacial energy and QCM-D measurements, whereas the CTAB adsorption at these concentrations does not result in the reduction of the COF. In contrast to $A_{q,SSP}$, the values of $A_{q,SPS}$ start to increase only in region 2, where the COF reduces rapidly with the increase in CTAB concentration. The signals in SPS polarization are very sensitive to the orientation of CTAB molecules, and the correlation between $A_{q,SPS}$ and COF suggests the importance of efficient monolayer packing in addition to the adsorbed mass of CTAB. Because the SFG signals are sensitive to both concentration and orientational order, the increase in SFG intensity indicates that the conformational order of the monolayer continues to evolve beyond C^*. Although we do not report the SFG data for CTAB adsorption at the PDMS-D$_2$O interface, we expect similar results to those observed on PETS. The changes in the interfacial energy and the QCM-D data are similar for PETS- and PDMS-coated substrates. A combination of macroscopic and spectroscopic measurements reveals the formation of well-packed adsorbed CTAB monolayers beyond C^* over hydrophobic surfaces.

Our attention turns to the changes in the water structure as we increase the concentration of CTAB (**Fig. 2C**). Before adsorption, the spectral feature of PETS-D$_2$O shows a strongly bonded D$_2$O peak (2400 cm^{-1}), consistent with the water spectra observed in contact with hydrophobic monolayers (**48**). Adsorption of CTAB changes the D$_2$O spectral features, showing a strong peak at 2410 cm^{-1} and a weaker peak at 2490 cm^{-1}, assigned to weakly coordinated or liquid-like water molecules (**49**). The magnitude of the 2490-cm^{-1} peak reduces as we increase the concentration from 0.005 to 0.9 mM. In region 3, only one sharp peak at 2410 cm^{-1} is observed at 5.0 mM, assigned to strongly coordinated or ice-like water molecules. This dominant peak for strongly coordinated D$_2$O due to the CTAB$_{headgroup}$-D$_2$O interaction is expected for an ordered monolayer, as a consequence of the increased surface charge (**22**). This orientation of water molecules next to lipid head groups has been observed with CARS as well (**27**). It is clear that the structure of water next to the CTAB monolayer continues to change from region 2 to region 3 as we increase the concentration of CTAB. A model, scaled to the dimensions based on the QCM-D, SFG spectroscopy, and previous calculations (**1**, **36**), for a complete CTAB-adsorbed monolayer is, shown in **Fig. 2E**.

SFG has complemented adsorption measurements by providing molecular details of the structure and orientation of CTAB and water molecules at the hydrophobic interface before contact is established. A monolayer is formed in a perpendicular orientation (**45**). The orientation of ordered water molecules is likely to be with the hydrogen atoms pointing away from the positively charged CTAB head group, as suggested by phase-sensitive heterodyne SFG (**50**). The structure of water is similar to that observed for a charged interface and evolves with the adsorption of surfactant beyond C^*. These molecular details explain the qualitative trends of COF.

A direct comparison between adhesion and COF with the adsorption isotherm of surfactants reveals clear gaps in our understanding of the changes in sliding friction and zero-load adhesion values (text S6). As shown in **Fig. 1A**, the zero-load adhesion values at low CTAB concentrations are higher than those measured in air, indicating a dry contact (**30**). Beyond 0.005 mM, no adhesion was measurable using this technique. This indicates that interstitial water is not getting squeezed out at these concentrations. At these low concentrations in region 1, the interfacial energy is insensitive to the changes. In contrast, using QCM-D and SFG, we detect the presence of CTAB molecules in contact with PETS at low concentrations. The adhesion data cannot be explained on the basis of adsorption results alone, and they do not reconcile our understanding of the COF measurements either.

In region 1, we have observed adsorption of surfactants but anticipated dry contact based on the high COF values, which is comparable to the dry PDMS-PETS contact (**Fig. 1D**). In region 2, surfactant adsorption on the surfaces can potentially hold a fluid layer in the gap to ease the sliding friction. In region 3, we identify the surfaces to be covered with CTAB monolayers and expect the COF not to change any further. However, this is not what is observed in the experimental results. Although the SFG spectra for CTAB on PETS have suggested enhancement in CTAB ordering and corresponding water structure beyond C^*, they are not a true representation of the two contacting interfaces. We expect a fluid layer between the confined surfaces. An important question is what the nature is of the fluid layer that differentiates regions 2 and 3 if we suspect that water prevents contact between the two surfaces. The differences between regions 2 and 3 could be due to the difference in the physical properties of the interstitial fluid, such as loose surfactant molecules on top of the rigidly adsorbed film. However, this conjecture could not be verified without spectroscopy. In region 3, the COF is low but not low enough for what is expected from a hydrodynamic lubricating liquid layer. The results shown in **Fig. 1** are not sufficient to explain low COF in region 3. Although general qualitative conclusions can be drawn to explain the COF based on adsorbed CTAB, a direct probing of the contact interface is necessary.

Figure 3A shows the SFG spectra for the PDMS-PETS interface in dry and underwater contact as a function of CTAB concentration. In SFG experiments, we are using a larger contact spot (area, 2.3 mm^2; P = 1 MPa) to assure that the laser beam spot probes only the contact zone. This additional pressure does not have any drastic effect on the estimated thickness of confined water, as will be discussed later. A PDMS-PETS contact spectrum under dry conditions shows two additional peaks, 2900 and 2965 cm^{-1}, assigned to Si-CH$_{3,sym}$ and Si-CH$_{3,asym}$, respectively, in addition to the phenyl peak of PETS (**51**, **52**). The SFG spectra in the hydrocarbon region with adsorbed CTAB do not appear to be any different from the control without CTAB. At a first glance, this would suggest that the adsorbed CTAB molecules are squeezed out from the gap under pressure. However, we expect that the adsorbed CTAB molecules cover both the PDMS and PETS surfaces. With an interference SFG model, the calculations show weak hydrocarbon signals due to the destructive interference between the CTAB monolayer adsorbed on PETS surface and the oppositely oriented CTAB layer adsorbed on PDMS surface (text S7). SFG signals do not cancel for separations greater than 400 nm. We estimate that the SFG intensity can drop by two orders of magnitude because of the destructive interference from the two layers with opposite orientation under confinement. The lack of a strong SFG signal corresponding to CTAB molecules under confinement also reveals that there are no loosely adsorbed surfactant molecules in the gap that could influence the sliding friction. The absence of any loose surfactants present in the gap and the applied pressures that overcome DLVO repulsive forces point to hydration forces as the cause for lower COF in region 3. The presence of interstitial water can be confirmed with SFG.

⬇ Download high-res image   ⬈ Open in new tab   ⬇ Download Powerpoint

Science Advances

(B) regions. (**C**) An increase in ordering of strongly coordinated interfacial water ($A_{q,2390}$) is compared with COF with surfactant addition, in which the water peak continues to increase past C*. The characteristic regions (1 to 3) from the adsorption isotherm are indicated by the vertical bars. (**D**) Schematic for probing the contact interface in total internal reflection geometry. The flattening of the lens under repulsive loads is accentuated for clear visualization. ω_{Vis} and ω_{IR} indicate the frequencies of visible and infrared laser beams, respectively. (**E**) Depiction of confined D_2O arranged between two saturated hydrophobic surfaces with CTAB in region 3. The arrangement captures confined strongly coordinated water at the repulsive contact interface between cationic head groups.

We observed some striking changes in the D_2O signals at the contact interface (2250 to 2800 cm^{-1}). D_2O is absent for PDMS-PETS contact in air and underwater. This lack of signal could result from the cancellation of the water signals due to destructive interference. However, considering the observation that the work of adhesion and friction are high, the low D_2O signals are more likely due to dry contact rather than the interference effect (**30**). The lack of D_2O signal confirms the fact that SFG is not probing the liquid water outside the contact zone. At 0.005 mM CTAB, the spectral features for D_2O are not discernible. If any water is present, it has minimal effect on adhesion and friction. In regions 2 and 3, clear D_2O peaks are observed at the contact interface. At 0.1 mM, a weak D_2O peak is observed at 2420 cm^{-1}; however, the friction is not reduced, suggesting the possibility of heterogeneous patchy contact (**48**). At high concentrations, only an intense peak around 2400 cm^{-1} appears, corresponding to strongly coordinated water, and the less coordinated water peak at 2490 cm^{-1} is not observed at the contact interface.

In **Fig. 3C**, we plot the value of $A_{q,2390}$ peak versus CTAB concentration. Again, we observe that in region 1, where the COF was high, the weakness of the D_2O peak amplitude suggests that there is some critical concentration or that an ordering of water is necessary for lowering the friction. The water peak increases in intensity, and a peak around 2390 cm^{-1} signifies ice-like coordinated water in region 2, whereas the COF drops consistently with increasing CTAB concentration. In region 3, the ice-like D_2O peak continues to increase, showing a strongly coordinated water structure (**27**) that results in the reduction of friction beyond C*.

The two concentrations, 0.1 and 5.0 mM CTAB, are of interest because water is present during static contact, but the magnitude of sliding friction is different. At 0.1 mM CTAB, the COF appears similar to that of dry contact, but we observed water signal in static contact. At 5.0 mM CTAB, the friction is lower and we anticipate water to still be present during sliding. To investigate whether the nature of interfacial static contact is maintained during sliding, we measured the changes in SFG intensity during sliding, as depicted by the schematic in **Fig. 4A**. At the start of these experiments, the PDMS lens is initially out of contact from the aligned laser beam spot and is then slid toward the interrogation zone at a speed of 5 μm/s. The incident angle was the same one used to probe the static contact between CTAB-covered PDMS and PETS surfaces. The changes in the SFG intensity for the 3050-cm^{-1} peak (PETS) during sliding are shown in **Fig. 4A**. The increase in intensity is due to changes in the Fresnel factors when we overlap the laser beam with the contact area of the PDMS lens. Because we expect the SFG signature of the PETS monolayer to not change during sliding, we can now compare the changes in the structure of CTAB and D_2O relative to PETS during sliding. The changes in intensity for 3050 cm^{-1} (PETS), 2935 cm^{-1} (CTAB), and 2410 cm^{-1} (highly coordinated ice-like D_2O) as a function of sliding time are shown in **Fig. 4** [B (0.1 mM CTAB) and C (5.0 mM CTAB)]. Because Fresnel factors change during sliding, we can only quantify the changes in the structure by comparing the SFG intensity of the CTAB and D_2O peaks with that of PETS when the laser beams are overlapped with the center of contact area. These SFG intensity ratios during sliding contact are compared with those observed for static contact (**Fig. 3**, A and B). The results for the 0.1 mM and 5.0 mM CTAB concentrations are shown in **Fig. 4D**. Although there were differences in the SFG intensity sliding profile, the signals for the ice-like D_2O peak and the CTAB peak are similar for static and sliding contact after normalization. This suggests that at 0.1 mM, the high COF is not due to the squeezing out of interstitial water but perhaps to a patchy contact between the incompletely covered PETS and PDMS surfaces. For 5 mM CTAB, the strong ice-like water structure is maintained during sliding, resulting in a low COF. The drop in CTAB intensity during sliding (**Fig. 4**, B and C) is consistent with our observation from static contact experiments, where we have observed a cancellation of the SFG signals due to the oppositely oriented CTAB monolayers. These results provide convincing evidence that the CTAB monolayers are not perturbed during sliding. Above cmc, it is possible that there could be micelles trapped within the contact zone, which may affect the friction coefficient. However, SFG spectroscopy is very sensitive to the breakdown in orientational symmetry, and we have not observed any differences in the SFG spectra (static and sliding contact) corresponding to the CTAB vibrational bands. Therefore, it is unlikely for trapped micellar structures (diameter, 8 nm) (**53**) to be present within the gap, and the results support the presence of only water between the two oppositely oriented CTAB monolayers sliding past each other. The similarity between the intensity ratios for static and sliding contact suggests that the inferences based on a detailed spectral analysis for static contact also represent the molecular picture during sliding.

⬇ Download high-res image　　⬀ Open in new tab　　⬇ Download Powerpoint

Fig. 4 The underwater contact interface probed during sliding using SFG spectroscopy.

The contact interface probed during sliding using SFG spectroscopy for PDMS-PETS underwater contact using D_2O in the presence of CTAB. The measurements were done in SSP polarization at an incident angle of 8°. (**A**) A schematic for a sliding experiment where the PDMS lens is initially outside the contact zone of the interrogating aligned laser beams. The lens is then slid into contact and then out of contact at 5 μm/s. (**B** and **C**) Traces for the changing absolute SFG intensity, not the Lorentzian peak amplitude, for PETS (3050 cm^{-1}), CTAB (2935 cm^{-1}), and ice-like D_2O (2410 cm^{-1}) peaks with sliding in the presence of (B) 0.1 mM CTAB and (C) 5.0 mM CTAB. (**D**) Comparison of the normalized SFG intensities of CTAB and D_2O peaks by PETS peak intensity in static and sliding contact. The intensity as a function of time during sliding is averaged when the laser beams are overlapped with the center of contact area. Error bars are evaluated from at least three static spectral intensities and two sliding scans.

We would like to summarize the results by putting several intriguing and unresolved observations into perspective. First, we can estimate the thickness of the hydration layer separating the two charged surfaces by comparing our applied normal pressure (~100 kPa for friction and 1

force law (text S8) (55). For partial coverage (region 2), we expect the thickness of the confined water layer to be less than 2 nm and perhaps nonuniform or patchy as the SFG friction experiments indicate. For low coverage, the two surfaces make dry contact.

Although the COF is reduced at high surfactant concentrations, it is not as low as expected for the sliding between two surfaces separated by 2 to 4 nm of liquid water (13). Using 2- to 4-nm-thick water layer, sliding velocity of 5 µm/s (shear rate of 1250 to 2500 s^{-1}), and shear stress of ~2 × 10^4 at ~1-mN applied load, we calculate an effective viscosity of ≈10 Pa·s. This is four orders of magnitude higher than the viscosity of bulk water. The confined water consists of a mixture of water, charged head groups, counterions, and added salt ions. The high effective viscosity measured here reflects the viscosity of this complex confined interlayer. Higher effective viscosity of confined water has been reported using SFA for confined salt water between two mica surfaces (12, 56). MD simulations have also observed longer relaxation times of water confined between surfactant assemblies (57, 58). The concept of a protrusion layer (steric) and the ionic head groups mixed with the water layer could also result in enhanced dissipation because of the sliding of these head groups across each other, resulting in a higher effective viscosity. There is a need to develop a theoretical framework based on MD simulations to understand the viscosity of this confined aqueous layer between two charged surfaces.

Here, we find that the frictional stress is linearly proportional to the normal load. After the shear forces were normalized with the contact area, the shear stress is also observed to be a function of normal load. This linear dependence has also been observed for surfactant-coated atomically smooth mica surfaces in dry contact (59). Here, it could be related to damage or wear of the CTAB monolayers. However, the SFG friction experiments show that the contact interface is not affected by sliding, and therefore, damage of the monolayers is not the reason behind this linearity. The changes in thickness and viscosity of the confined water layer with pressure could perhaps result in the interlayer slip (5) that occurs during sliding and causes the linear dependence of shear stress on normal load.

The most intriguing observation is the non-zero SFG signal related to confined water. For two CTAB-covered surfaces in close contact with each other, we have not observed any discernible SFG signatures assignable to the CTAB monolayer, as observed when the two surfaces are out of contact. The SFG signals for CTAB monolayer are canceled because of the symmetry that occurs from the oppositely oriented CTAB monolayers in contact. Likewise, we had anticipated that the D$_2$O peaks should also be absent upon contact. MD results showed two oppositely oriented identical water layers between two fatty alcohol–coated surfaces, which would result in the absence of SFG signal for confined water (60). There are three possible explanations for a non-zero D$_2$O signal. First, the two CTAB layers (one on PDMS and the other on PETS-SAM) are not exactly identical, and the SFG signals from these two oppositely oriented water layers do not cancel each other. Because we cannot directly compare the SFG amplitude strength between hydrocarbon and D$_2$O regions, we have calculated the ratio of D$_2$O amplitude strength ($A_{q,2390}$) to that of PETS (phenyl) monolayer ($A_{q,3050}$) before (0.6) and during contact (4.5). That this ratio is higher during contact indicates an enhancement in water ordering, and these calculations do not support the idea of partial cancellation due to imperfect monolayers. The second reason could be due to inherent breakdown in the centrosymmetry of confined water, triggered by the strong hydration of charged head groups and counterions (Br$^-$ from CTAB and Cl$^-$ from NaCl). Finally, it is possible that water percolated through one of the CTAB monolayers and came in contact with the underlying hydrophobic (PDMS or PETS) layers, resulting in a highly coordinated water structure. However, this also required both surfaces to be different; otherwise, the SFG signals should cancel out due to symmetry. Although we do not offer an explanation for noncentrosymmetric water signal, our results reveal an intricate state of confined water layer between two charged surfaces, resulting in strong hydration forces, higher effective viscosity, and a highly coordinated hydrogen bonding network, which is a characteristic of ice.

CONCLUSIONS

By combining adhesion and friction experiments with surface sensitive spectroscopy, we demonstrated the intricate role of surface charge and ordered water in controlling hydration forces and friction coefficients. To our knowledge, these results reveal, for the first time, a highly coordinated ice-like water layer between two surfactant-covered surfaces that withstands confinement pressures and reduces sliding friction. Although the reduction in COF was expected upon adding surfactant molecules, we find two intriguing surprises at low and high surfactant concentrations. Almost 70% of surfactant coverage is ineffective in reducing COF, even though we observe the presence of confined water between the charged head groups. This indicates that a minimum quantity of charged head groups is necessary to hold water at these normal loads to reduce the COF. Surprisingly, even after achieving the complete monolayer coverage, the COF continues to decrease and is accompanied by changes in the structure of highly coordinated confined water.

The observation of a strong signal for confined deuterated water is surprising, and this indicates that the confined water layer has noncentrosymmetric structure. The relative intensity of water signals in comparison to the ordered PETS monolayer indicates that this signal cannot be due to the differences in the structure of water from the two contacting surfaces. The SFG signals during sliding were comparable to those collected in static contact, indicating that the structure of the ordered fluid is maintained during sliding. More detailed MD simulations are needed to elucidate the origin behind these water signals and to understand where the sliding is taking place within the confined fluid.

Although the context of this work focuses on understanding adhesion and sliding friction, the packing and self-assembly of amphiphilic molecules and the water associated with the polar head groups govern interfacial processes in many different fields, most notably biology. One must now consider whether and how the structure of water promotes or inhibits interfacial phenomena, such as protein folding toward a specific conformation or the mediation in ligand binding for enzyme catalysis (61).

MATERIALS AND METHODS

Sample preparations

a piranha solution because it is extremely corrosive. The samples were rinsed with copious amounts of deionized water and plasma-treated

(PDC-32G, Harrick Scientific) for 5 min before SAM functionalization. After removal from solution, the substrates were rinsed with toluene and methanol, dried with N_2, and annealed under vacuum for 2 hours at 120°C. Cationic surfactant CTAB was triply recrystallized in ethanol/acetone (1:1) mixture, and the solutions were made with Millipore ultrapure water (~18.2 megohms). The conditions used in these measurements are below the solution saturation concentration (100 mM) at the Krafft point temperature for CTAB (**62**). All CTAB solutions contained 1 mM NaCl. The purity was confirmed by measuring the critical micellar concentration, 0.9 mM (**46**), using the Wilhelmy plate method.

Contact angle measurements

Contact angles were measured by monitoring sessile probe droplets of CTAB solutions with varying concentrations on hydrophobic surfaces using a Ramé-Hart goniometer. The changing contact angle values were recorded, corresponding to the CTAB adsorption from the probe droplet onto the hydrophobic surface, and the steady-state contact angle values were reported after 15 min of equilibrium adsorption. The substrates were enclosed under a transparent quartz cuvette to minimize the evaporation of probe droplets.

Friction measurements

Friction measurements were performed using a homebuilt biaxial friction cell as previously described (**48**). The sensors for both normal and shear force were calibrated using known weights in the range of 1 to 98 mN. After allowing 15 min of equilibrium adsorption of CTAB on PETS-SAM, a PDMS lens was brought in contact with the SAM substrate underwater at different normal loads (1 to 30 mN). These loads correspond to pressures of 10 to 100 kPa based on adhesion energies estimated using the Hertzian and JKR theories. An independent measurement using a force sensor and optical microscope supported our calculations. The lens was slid at a rate of 5 μm/s, using the Newport Optics Picomotor. Measurements were repeated at least three times on different substrates and contact spots.

QCM-D measurements

Adsorption of CTAB was quantified on PETS- and PDMS-coated surfaces using QCM-D (Q-Sense Model E4, Q-Sense AB). SiO_2-coated quartz sensors were functionalized with PETS by the procedure described earlier. PDMS at 0.5 wt % in hexane was spin-coated on undecanethiol functionalized gold-coated quartz sensors, resulting in a film thickness of around 50 nm. CTAB solutions were flowed over the sensors with increasing concentration in a sequential manner. Detailed experimental procedure was as described earlier (**63**).

SFG spectroscopy

SFG spectroscopy is a second-order nonlinear optical technique sensitive to the concentration and orientation of interfacial molecules. The details of SFG instrumentation have been described elsewhere (**30**). The incident angles for SAM-air, SAM-water, and SAM-PDMS contact interface were 42°, 16°, and 8°, respectively, with reference to the surface normal of an equilateral sapphire prism. The laser beam size was estimated to be 1 mm^2 focused over a contact spot area of 2.3 mm^2, when the lens was in mechanical contact. The applied pressure was ~1 MPa, calculated based on Hertzian contact mechanics and supported with an independent measurement of force and contact area. An equilibrium adsorption time of 15 min was allowed before the SFG spectra were collected.

SUPPLEMENTARY MATERIALS

Supplementary material for this article is available at **http://advances.sciencemag.org/cgi/content/full/2/8/e1600763/DC1**

text S1. Example of COF measurement.

text S2. Determination of interfacial energy, surface excess, and area per molecule from contact angle measurements.

text S3. Mass adsorption measured by QCM-D.

text S4. Raman and Fourier transform infrared (FTIR) spectra of PETS and CTAB.

text S5. SFG spectral fitting and peak assignment summary.

text S6. Adhesion energy measured by zero-load JKR measurements.

text S7. Fresnel factor calculations.

text S8. Calculation of water thickness between charged surfaces.

fig. S1. Shear force response to the normal loading in friction measurements.

fig. S2. Contact angle measurements with CTAB solutions on PETS and PDMS.

fig. S3. QCM-D data for CTAB adsorption on PETS and PDMS.

fig. S4. FTIR and Raman vibrational spectra.

fig. S5. JKR measurements for work of adhesion.

fig. S6. Calculations for the Fresnel factors in total internal refection geometry.

ScienceAdvances

This is an open-access article distributed under the terms of the **Creative Commons Attribution-NonCommercial license**, which permits use, distribution, and reproduction in any medium, so long as the resultant use is **not** for commercial advantage and provided the original work is properly cited.

REFERENCES AND NOTES

1. ↵ C. Tanford, *The Hydrophobic Effect: Formation of Micelles and Biological Membranes* (Wiley-Interscience, New York, ed. 2, 1980).

2. ↵ J. Israelachvili, R. Pashley, The hydrophobic interaction is long range, decaying exponentially with distance. *Nature* **300**, 341–342 (1982). CrossRef   PubMed   Google Scholar

3. M. S. Cheung, A. E. García, J. N. Onuchic, Protein folding mediated by solvation: Water expulsion and formation of the hydrophobic core occur after the structural collapse. *Proc. Natl. Acad. Sci. U.S.A.* **99**, 685–690 (2002). Abstract/FREE Full Text   Google Scholar

4. ↵ R. C. Rodrigues, C. Ortiz, Á. Berenguer-Murcia, R. Torres, R. Fernández-Lafuente, Modifying enzyme activity and selectivity by immobilization. *Chem. Soc. Rev.* **42**, 6290–6307 (2013). CrossRef   PubMed   Google Scholar

5. ↵ J. N. Israelachvili, *Intermolecular and Surface Forces* (Academic Press, Burlington, MA, ed. 3, 2011).

6. ↵ D. M. LeNeveu, R. P. Rand, Measurement and modification of forces between lecithin bilayers. *Biophys. J.* **18**, 209–230 (1977). CrossRef   PubMed   Web of Science   Google Scholar

7. J. N. Israelachvili, R. M. Pashley, Molecular layering of water at surfaces and origin of repulsive hydration forces. *Nature* **306**, 249–250 (1983). CrossRef   GeoRef   Web of Science   Google Scholar

8. ↵ J. N. Israelachvili, H. Wennerstroem, Entropic forces between amphiphilic surfaces in liquids. *J. Phys. Chem.* **96**, 520–531 (1992). CrossRef   Web of Science   Google Scholar

9. V. A. Parsegian, N. Fuller, R. P. Rand, Measured work of deformation and repulsion of lecithin bilayers. *Proc. Natl. Acad. Sci. U.S.A.* **76**, 2750–2754 (1979). Abstract/FREE Full Text   Google Scholar

10. O. Abillon, E. J. Perez, Swollen lamellar phases between two solid walls: Undulation forces and generation of defects. *J. Phys.* **51**, 2543–2556 (1990). Google Scholar

11. ↵ K. V. Damodaran, K. M. Merz, Head group-water interactions in lipid bilayers: A comparison between DMPC- and DLPE-based lipid bilayers. *Langmuir* **9**, 1179–1183 (1993). Google Scholar

12. ↵ A. Dhinojwala, S. Granick, Relaxation time of confined aqueous films under shear. *J. Am. Chem. Soc.* **119**, 241–242 (1997). Google Scholar

13. ↵ U. Raviv, J. Klein, Fluidity of bound hydration layers. *Science* **297**, 1540–1543 (2002). Abstract/FREE Full Text   Google Scholar

14. S. H. Khan, G. Matei, S. Patil, P. M. Hoffmann, Dynamic solidification in nanoconfined water films. *Phys. Rev. Lett.* **105**, 106101 (2010). CrossRef   PubMed   Google Scholar

15. ↵ S. H. Lee, P. J. Rossky, A comparison of the structure and dynamics of liquid water at hydrophobic and hydrophilic surfaces—A molecular dynamics simulation study. *J. Chem. Phys.* **100**, 3334 (1994). CrossRef   Web of Science   Google Scholar

16. ↵ D. E. Gragson, B. M. McCarty, G. L. Richmond, Ordering of interfacial water molecules at the charged air/water interface observed by vibrational sum frequency generation. *J. Am. Chem. Soc.* **119**, 6144–6152 (1997). CrossRef   Google Scholar

17. J. Fitter, R. E. Lechner, N. A. Dencher, Interactions of hydration water and biological membranes studied by neutron scattering. *J. Phys. Chem. B* **103**, 8036–8050 (1999). Google Scholar

18. L. Cheng, P. Fenter, K. L. Nagy, M. L. Schlegel, N. C. Sturchio, Molecular-scale density oscillations in water adjacent to a mica surface. *Phys. Rev. Lett.* **87**, 156103 (2001). CrossRef   PubMed   Google Scholar

19. J. J. Valle-Delgado, J. A. Molina-Bolívar, F. Galisteo-González, M. J. Gálvez-Ruiz, A. Feiler, M. W. Rutland, Hydration forces between silica surfaces: Experimental data and predictions from different theories. *J. Chem. Phys.* **123**, 034708 (2005). CrossRef   Google Scholar

20. ↵ T. G. Trudeau, K. C. Jena, D. K. Hore, Water structure at solid surfaces of varying hydrophobicity. *J. Phys. Chem. C* **113**, 20002–20008 (2009). Google Scholar

21. ↵ Q. Du, E. Freysz, Y. R. Shen, Vibrational spectra of water molecules at quartz/water interfaces. *Phys. Rev. Lett.* **72**, 238–241 (1994). CrossRef   PubMed   Web of Science   Google Scholar

23. P. B. Miranda, L. Xu, Y. R. Shen, M. Salmeron, Icelike water monolayer adsorbed on mica at room temperature. *Phys. Rev. Lett.* **81**, 5876–5879 (1998). CrossRef   Web of Science   Google Scholar

24. ↵ X. Chen, W. Hua, Z. Huang, H. C. Allen, Interfacial water structure associated with phospholipid membranes studied by phase-sensitive vibrational sum frequency generation spectroscopy. *J. Am. Chem. Soc.* **132**, 11336–11342 (2010). PubMed   Google Scholar

25. ↵ Q. Du, E. Freysz, Y. R. Shen, Surface vibrational spectroscopic studies of hydrogen bonding and hydrophobicity. *Science* **264**, 826–828 (1994). Abstract/FREE Full Text   Google Scholar

26. ↵ S. Nihonyanagi, K. Uosaki, Sum frequency generation (SFG) study of the pH-dependent water structure on a fused quartz surface modified by an octadecyltrichlorosilane (OTS) monolayer. *Phys. Chem. Chem. Phys.* **3**, 3463–3469 (2001). CrossRef   Web of Science   Google Scholar

27. ↵ J.-X. Cheng, S. Pautot, D. A. Weitz, X. S. Xie, Ordering of water molecules between phospholipid bilayers visualized by coherent anti-Stokes Raman scattering microscopy. *Proc. Natl. Acad. Sci. U.S.A.* **100**, 9826–9830 (2003). Abstract/FREE Full Text   Google Scholar

28. ↵ Q. Du, X.-d. Xiao, D. Charych, F. Wolf, P. Frantz, Y. R. Shen, M. Salmeron. Nonlinear optical studies of monomolecular films under pressure. *Phys. Rev. B Condens. Matter* **51**, 7456–7463 (1995). PubMed   Google Scholar

29. ↵ S. C. Richards, A. D. Roberts, Boundary lubrication of rubber by aqueous surfactant. *J. Phys. D Appl. Phys.* **25**, A76 (1992). CrossRef   Google Scholar

30. ↵ A. P. Defante, T. N. Burai, M. L. Becker, A. Dhinojwala, Consequences of water between two hydrophobic surfaces on adhesion and wetting. *Langmuir* **31**, 2398–2406 (2015). CrossRef   PubMed   Google Scholar

31. ↵ J. R. Lu, M. Hromadova, E. A. Simister, R. K. Thomas, J. Penfold, Neutron reflection from hexadecyltrimethylammonium bromide adsorbed at the air/liquid interface: The variation of the hydrocarbon chain distribution with surface concentration. *J. Phys. Chem.* **98**, 11519–11526 (1994). Google Scholar

32. ↵ S. Bandyopadhyay, J. C. Shelley, M. Tarek, P. B. Moore, M. L. Klein, Surfactant aggregation at a hydrophobic surface. *J. Phys. Chem. B* **102**, 6318–6322 (1998). Google Scholar

33. ↵ H. Haidara, M. K. Chaudhury, M. J. Owen, A direct method of studying adsorption of a surfactant at solid-liquid interfaces. *J. Phys. Chem.* **99**, 8681–8683 (1995). Google Scholar

34. ↵ R. M. Pashley, P. M. McGuiggan, R. G. Horn, B. W. Ninham, Forces between bilayers of cetyltrimethylammonium bromide in micellar solutions. *J. Colloid Interface Sci.* **126**, 569–578 (1988). CrossRef   Web of Science   Google Scholar

35. ↵ S. Prasad, H. Zhu, A. Kurian, I. Badge, A. Dhinojwala, Interfacial segregation in polymer blends driven by acid–base interactions. *Langmuir* **29**, 15727–15731 (2013). Google Scholar

36. ↵ G. C. McGonigal, R. H. Bernhardt, D. J. Thomson, Imaging alkane layers at the liquid/graphite interface with the scanning tunneling microscope. *Appl. Phys. Lett.* **57**, 28–30 (1990). CrossRef   Web of Science   Google Scholar

37. ↵ D. Hankins, J. W. Moskowitz, F. H. Stillinger, Water molecule interactions. *J. Chem. Phys.* **53**, 4544–4554 (1970). CrossRef   Google Scholar

38. ↵ G. V. Gibbs, M. M. Hamil, S. J. Louisnat, L. S. Bartell, H. Yow, Correlations between Si-O bond length, Si-O-Si bond angle and bond overlap populations calculated using extended Hückel molecular orbital theory. *Am. Mineral.* **57**, 1578–1613 (1972). GeoRef   Web of Science   Google Scholar

39. ↵ P. D. Jadzinsky, G. Calero, C. J. Ackerson, D. A. Bushnell, R. D. Kornberg, Structure of a thiol monolayer-protected gold nanoparticle at 1.1 Å resolution. *Science* **318**, 430–433 (2007). Abstract/FREE Full Text   Google Scholar

40. ↵ P. Guyot-Sionnest, J. H. Hunt, Y. R. Shen, Sum-frequency vibrational spectroscopy of a Langmuir film: Study of molecular orientation of a two-dimensional system. *Phys. Rev. Lett.* **59**, 1597–1600 (1987). CrossRef   PubMed   Web of Science   Google Scholar

41. ↵ K. S. Gautam, A. D. Schwab, A. Dhinojwala, D. Zhang, S. M. Dougal, M. S. Yeganeh, Molecular structure of polystyrene at air/polymer and solid/polymer interfaces. *Phys. Rev. Lett.* **85**, 3854–3857 (2000). CrossRef   PubMed   Web of Science   Google Scholar

42. ↵ S. Dzwigaj, A. de Mallmann, D. Barthof, Adsorption of benzene and ethylbenzene on the acidic and basic sites of β zeolite. *J. Chem. Soc. Faraday Trans.* **86**, 431–435 (1990). Google Scholar

43. ↵ R. A. Walker, J. C. Conboy, G. L. Richmond, Molecular structure and ordering of phospholipids at a liquid-liquid interface. *Langmuir* **13**, 3070–3073 (1997). CrossRef   Web of Science   Google Scholar

44. ↵ J. C. Conboy, M. C. Messmer, G. L. Richmond, Investigation of surfactant conformation and order at the liquid-liquid interface by total internal reflection sum-frequency vibrational spectroscopy. *J. Phys. Chem.* **100**, 7617–7622 (1996). CrossRef   Web of Science   Google Scholar

45. ↵ C. D. Bain, P. B. Davies, T. H. Ong, R. N. Ward, M. A. Brown, Quantitative analysis of monolayer composition by sum-frequency vibrational spectroscopy. *Langmuir* **7**, 1563–1566 (1991). CrossRef   Web of Science   Google Scholar

46. ↵ R. A. Campbell, S. R. W. Parker, J. P. R. Day, C. D. Bain, External reflection FTIR spectroscopy of the cationic surfactant hexadecyltrimethylammonium bromide (CTAB) on an overflowing cylinder. *Langmuir* **20**, 8740–8753 (2004). CrossRef   PubMed   Google Scholar

47. ↵ J. T. Edsall, Raman spectra of amino acids and related substances. III. Ionization and methylation of the amino group. *J. Chem. Phys.* **5**, 225–237 (1937). CrossRef   Google Scholar

48. ↵ K. Nanjundiah, P. Y. Hsu, A. Dhinojwala, Understanding rubber friction in the presence of water using sum-frequency generation spectroscopy. *J. Chem. Phys.* **130**, 024702 (2009). CrossRef   PubMed   Google Scholar

50. ↵ S. Nihonyanagi, S. Yamaguchi, T. Tahara, Direct evidence for orientational flip-flop of water molecules at charged interfaces: A heterodyne-detected vibrational sum frequency generation study. *J. Chem. Phys.* **130**, 204704 (2009). CrossRef PubMed Google Scholar

51. ↵ C. Chen, J. Wang, Z. Chen, Surface restructuring behavior of various types of poly (dimethylsiloxane) in water detected by SFG. *Langmuir* **20**, 10186–10193 (2004). PubMed Google Scholar

52. ↵ B. Yurdumakan, G. P. Harp, M. Tsige, A. Dhinojwala, Template-induced enhanced ordering under confinement. *Langmuir* **21**, 10316–10319 (2005). CrossRef PubMed Google Scholar

53. ↵ P. S. Goyal, B. A. Dasannacharya, V. K. Kelkar, C. Manohar, K. S. Rao, B. S. Valaulikar, Shapes and sizes of micelles in CTAB solutions. *Phys. B* **174**, 196–199 (1991). Google Scholar

54. ↵ R. M. Pashley, J. N. Israelachvili, A comparison of surface forces and interfacial properties of mica in purified surfactant solutions. *Colloids Surf.* **2**, 169–187 (1981). CrossRef Google Scholar

55. ↵ S. Leikin, V. A. Parsegian, D. C. Rau, R. P. Rand, Hydration forces. *Annu. Rev. Phys. Chem.* **44**, 369–395 (1993). CrossRef PubMed Web of Science Google Scholar

56. ↵ L. Ma, A. Gaisinskaya-Kipnis, N. Kampf, J. Klein, Origins of hydration lubrication. *Nat. Commun.* **6**, 6060 (2015). Google Scholar

57. ↵ P. A. Pieniazek, Y.-S. Lin, J. Chowdhary, B. M. Ladanyi, J. L. Skinner, Vibrational spectroscopy and dynamics of water confined inside reverse micelles. *J. Phys. Chem. B* **113**, 15017–15028 (2009). PubMed Google Scholar

58. ↵ S. Roy, D. Skoff, D. V. Perroni, J. Mondal, A. Yethiraj, M. K. Mahanthappa, M. T. Zanni, J. L. Skinner, Water dynamics in gyroid phases of self-assembled gemini surfactants. *J. Am. Chem. Soc.* **138**, 2472–2475 (2016). Google Scholar

59. ↵ H. Yoshizawa, Y. L. Chen, J. Israelachvili, Fundamental mechanisms of interfacial friction. 1. Relation between adhesion and friction. *J. Phys. Chem.* **97**, 4128–4140 (1993). CrossRef Web of Science Google Scholar

60. ↵ M. Ø. Jensen, O. G. Mouritsen, G. H. Peters, The hydrophobic effect: Molecular dynamics simulations of water confined between extended hydrophobic and hydrophilic surfaces. *J. Chem. Phys.* **120**, 9729–9744 (2004). CrossRef PubMed Google Scholar

61. ↵ P. Ball, Water as an active constituent in cell biology. *Chem. Rev.* **108**, 74–108 (2008). CrossRef PubMed Web of Science Google Scholar

62. ↵ J. Ž. Manojlović, The Krafft temperature of surfactant solutions. *Therm. Sci.* **16**, 631–640 (2012). Google Scholar

63. ↵ N. Dhopatkar, J. H. Park, K. Chari, A. Dhinojwala, Adsorption and viscoelastic analysis of polyelectrolyte–surfactant complexes on charged hydrophilic surfaces. *Langmuir* **31**, 1026–1037 (2015). Google Scholar

64. ↵ K. L. Johnson, K. Kendall, A. D. Roberts, Surface energy and the contact of elastic solids. *Proc. Math. Phys. Eng. Sci.* **324**, 301–313 (1971). Abstract/FREE Full Text Google Scholar

65. ↵ G. Li, A. Dhinojwala, M. S. Yeganeh, Interference effect from buried interfaces investigated by angular-dependent infrared–visible sum frequency generation technique. *J. Phys. Chem. C* **115**, 7554–7561 (2011). Google Scholar

View Abstract

We recommend

Controlling liquid splash on superhydrophobic surfaces by a vesicle surfactant
Meirong Song et al., Sci Adv, 2017

Electrostatic cloaking of surface structure for dynamic wetting
Satoshi Nita et al., Sci Adv, 2017

Ice-nucleating bacteria control the order and dynamics of interfacial water.
Ravindra Pandey et al., Sci Adv, 2016

Pt monolayer coating on complex network substrate with high catalytic activity for the hydrogen evolution reaction.
Man Li et al., Sci Adv, 2015

Electrolytes induce long-range orientational order and free energy changes in the H-bond network of bulk water.
Yixing Chen et al., Sci Adv, 2016

Boundary flow of water on supported phospholipid films
B. Cross et al., Europhys Lett, 2006

Semi-analytical method of calculating the electrostatic interaction of colloidal solutions*
Hongqing Tian et al., Chinese Physics B, 2017

Analysis of the induction of the myelin basic protein binding to the plasma membrane phospholipid monolayer*
Lei Zhang et al., Chinese Physics B, 2016

Behavior of lysozyme adsorbed onto biological liquid crystal lipid monolayer at the air/water interface*
Xiaolong Lu et al., Chinese Physics B, 2016

Non-exponential kinetic behaviour of confined water
P. Gallo et al., Europhys Lett

Powered by **Trend MD**

Science Advances

Science Advances

View this article with *LENS*

ARTICLE TOOLS

- Email
- Print
- Figures & Data
- Alerts
- Info & Metrics
- Citation tools
- eLetters
- PDF

- Download Powerpoint
- Save to my folders
- Request permissions
- Share

SIMILAR ARTICLES IN:

- Google Scholar

CITING ARTICLES IN:

- Web of Science (2)

Related Jobs

University

Zhenjiang, Jiangsu │ Salary Negotiable

Jiangsu University (JSU) is a comprehensive university especially reputed for its strength in engineering.

Employer: Jiangsu University

Group Leader Positions at National Institute of Biological Sciences, Beijing

7 Science Park Road, ZGC Life Science Park, Beijing Internationally-competitive salarie+renewable stable funding blocks that cover 5 year periods

Ambitious candidates looking to make high-impact discoveries and exhibiting a high probability of producing creative research are welcomed to apply.

Employer: National Institute of Biological Science, Beijing

Post-doc research fellow

Padua (IT) │ The salary of the Principal Investigator will be up to a maximum of € 33,000/year (gross amount)

We fund research projects for the duration of two years, proposed by researchers willing to launch an independent research in Padova.

Employer: Università di Padova

MORE JOBS ▶

Science

12 May 2017

Vol 356, Issue 6338

FEATURE

Where have all the insects gone?

DATA PRIVACY

Myriad take two: Can genomic databases remain secret?

BIOSECURITY

Biodefense in the 21st century

SCI COMMUN

News at a glance

CLIMATE CHANGE

Saying goodbye to glaciers

WORKING LIFE

Lucking into science

Table of Contents

Science Advances

Subscribe Today

Receive a year subscription to *Science* plus access to exclusive AAAS member resources, opportunities, and benefits.

First Name

Last Name

Email Address

Subscribe Today

Get Our Newsletters

Enter your email address below to receive email announcements from Science. We will also send you a newsletter digest with the latest published articles. See full list

- ☑ *Science* Advances TOC
- ☑ *Science* Table of Contents
- ☑ *Science* Daily News
- ☑ *Science* News This Week
- ☑ *Science* Editor's Choice
- ☑ First Release Notification

Email address

Sign up today

About us
About journals
Leadership
Team members
Work at AAAS

Advertise
Advertising kits
Custom publishing

For subscribers
Site license info
For members

International
Chinese
Japanese

Help
Access & subscriptions
Reprints & permissions
Contact us
Accessibility

Stay Connected

Terms of Service

Privacy Policy

Contact Us